



# Batteries & Supercaps

 **Chemistry  
Europe**  
European Chemical  
Societies Publishing

## Accepted Article

**Title:** A mapping of the physical and electrochemical properties of composite Lithium-ion batteries anodes made from graphite, Sn and Si

**Authors:** Sacha Smrekar, María Victoria Bracamonte, Emiliano N. Primo, Guillermina L. Luque, Jorge Thomas, Daniel E. Barraco, and Ezequiel Leiva

This manuscript has been accepted after peer review and appears as an Accepted Article online prior to editing, proofing, and formal publication of the final Version of Record (VoR). This work is currently citable by using the Digital Object Identifier (DOI) given below. The VoR will be published online in Early View as soon as possible and may be different to this Accepted Article as a result of editing. Readers should obtain the VoR from the journal website shown below when it is published to ensure accuracy of information. The authors are responsible for the content of this Accepted Article.

**To be cited as:** *Batteries & Supercaps* 10.1002/batt.202000096

**Link to VoR:** <https://doi.org/10.1002/batt.202000096>

WILEY-VCH

# A mapping of the physical and electrochemical properties of composite Lithium-ion batteries anodes made from graphite, Sn and Si

Sacha Smrekar,<sup>[a, b]</sup> M. Victoria Bracamonte,<sup>\*[a, b]</sup> Emiliano N. Primo,<sup>\*[a, b]</sup> Guillermina L. Luque,<sup>[c, d]</sup> Jorge Thomas,<sup>[e]</sup> Daniel E. Barraco,<sup>[a, b]</sup> Ezequiel Leiva<sup>[c, d]</sup>

- [a] S. Smrekar, Dr. M. V. Bracamonte, Dr. E. N. Primo, Prof. Dr. D. E. Barraco  
Facultad de Matemática Astronomía Física y Computación, Universidad Nacional de Córdoba  
Ciudad Universitaria, X5000HUA Córdoba, Argentina
- [b] S. Smrekar, Dr. M. V. Bracamonte, Dr. E. N. Primo, Prof. Dr. D. E. Barraco  
Instituto de Física Enrique Gaviola (IFEG - CONICET)  
Ciudad Universitaria, X5000HUA Córdoba, Argentina
- [c] Prof. Dr. G. L. Luque, Prof. Dr. E. Leiva  
Departamento de Química Teórica y Computacional  
Facultad de Ciencias Químicas, Universidad Nacional de Córdoba  
Ciudad Universitaria, X5000HUA Córdoba, Argentina
- [d] Prof. Dr. G. L. Luque, Prof. Dr. E. Leiva  
Instituto de Investigación en Físico Química de Córdoba (INFIQC - CONICET)  
Ciudad Universitaria, X5000HUA Córdoba, Argentina
- [e] Prof. Dr. J. Thomas  
YPF Tecnología S.A., Av. Del Petróleo S/N (e/129 y 143), 1923 Berisso, Buenos Aires, Argentina

Supporting information for this article is given via a link at the end of the document.

**Abstract:** Nowadays, there is an evident need to improve the current Li-ion battery systems, in order to make them more reliable, durable and safe. Regarding this objective, the application of composite materials –based mainly on the combination of Si, Sn and carbon– appears as a very promising alternative for future anode materials. However, despite the great amount of publications dealing with this topic, there is not a systematic study that allows interpreting and understanding how the combination of these materials affects the electrochemical performance of the anodes prepared with them. In light of this necessity, in this work we propose a straightforward ball-milling procedure to prepare Sn/Si/graphite composites with different mass proportions of each material. For all compositions, a systematic study was performed in order to determine how each material affects the specific capacity, capacity fading and stability towards a change in loading current. It is concluded that the material prepared with Sn<sub>33</sub>Si<sub>33</sub>C<sub>33</sub> appears to be the most promising one, delivering a reversible capacity of 906.9 mAh g<sup>-1</sup> even after 120 cycles at 0.5 A g<sup>-1</sup>, thus encouraging the development of new composites based on these materials for industrial applications.

## Introduction

Nowadays, lithium ion batteries (LIBs) are the most widespread electrochemical storage-based system due to their performance characteristics, capital requirements, safety and reliability.<sup>[1–4]</sup> However, conventional LIBs using graphite as anode (with a specific capacity of 372 mAh g<sup>-1</sup>), fail to meet the continuously increasing demand for high-output devices. For this reason, many research studies have focused on the development of new materials with higher energy densities – such as Li metal<sup>[5,6]</sup>, transition metal oxides<sup>[7–9]</sup>, Si<sup>[10–13]</sup> and Sn<sup>[14–16]</sup>. The two latter belong to the alloy-based negative active materials and had attracted much attention due to its high capacities and lower lithiation/delithiation potentials.<sup>[17]</sup>

Si has been regarded as one of the most promising candidates due to its abundant availability, high gravimetric capacity (3579 mAh g<sup>-1</sup>) and ideal electrochemical alloying/dealloying potential (lower than 0.5 V vs Li/Li<sup>+</sup>)<sup>[18]</sup>. However, Si has two main drawbacks for its commercial application: i) its large volume expansion (360 % for Li<sub>4.4</sub>Si) during full lithiation, which results in a low mechanical stability, capacity fading and short durability, and ii) its low intrinsic electronic conductivity.<sup>[19]</sup> In order to overcome these issues,

several authors have tested strategies such as coating Si with carbonaceous matrices<sup>[20–26]</sup> and reducing the Si particle size to the nanoscale.<sup>[27–29]</sup>

Recently, Si-metal alloys/composites including active or inactive metal matrices as buffer materials have been widely studied. Among these, Sn has drawn great attention due to its high conductivity and natural abundance. Sn can store up to 4.4 Li per Sn atom during lithiation, resulting in a theoretical capacity of 994 mAh g<sup>-1</sup>.<sup>[30]</sup> Unfortunately, Sn also suffers from large volume changes as Si, so their combination presents the same challenges as the pristine materials.

In order to solve these problems Yang et al.<sup>[18]</sup> proposed a Si<sub>0.40</sub>/Sn<sub>0.55</sub>@C-G<sub>0.05</sub> composite material, exhibiting a relative high initial coulombic efficiency of 81.5 % and a stable reversible capacity of 612.6 mAh g<sup>-1</sup> after 100 cycles at 0.10 Ag<sup>-1</sup>. The authors demonstrated that the presence of Sn acts as an active matrix, not only increasing the conductivity of the composite, but also decreasing the polarization resistance of the material. Similar results were previously obtained by Kawasaki et al.<sup>[33]</sup>, who synthesized a nanocomposite based on Si-Sn/reduced graphene oxide. The materials were prepared by a solution route resulting in a composite with Si:Sn:C composition of 14:3.5:100. The as-prepared material presents an initial specific capacity of 470 mAh g<sup>-1</sup> and a final capacity of 90 mAh g<sup>-1</sup> after 30 cycles. Al-Maghrabi et al.<sup>[34]</sup> studied the role played by carbon in the study of pseudo-binary libraries of the Sn-Si-C system. The samples were produced by sputtering, obtaining stratified structures. The authors concluded that, by increasing the carbon content, the tin grains aggregation was inhibited in these kind of thin-layered structures. When large amounts of carbon and silicon are present, the capacity is lower than that expected based on full reaction of Si, Sn and C with Li, suggesting the formation of nanoscale SiC. On other hand, Rock and Kumta<sup>[35]</sup> dispersed a Si<sub>0.66</sub>Sn<sub>0.34</sub> composite alloy (15 wt%) in a carbon (85 wt%) matrix using high-energy mechanical milling. The resultant

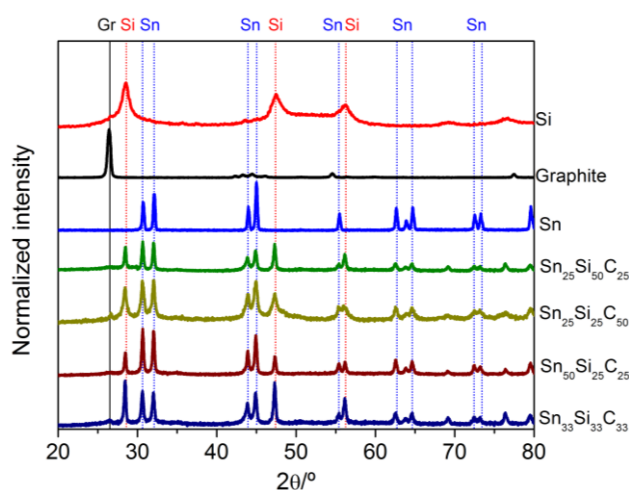
composites exhibited a reversible discharge capacity of 800 mAh g<sup>-1</sup> with capacity retention of 1.36 % loss/cycle. Xu et al.<sup>[30]</sup> synthesized Si-Sn-C nanocomposites by mechanical milling, analyzing the effect of the milling time on the phase composition and morphology of the studied samples. They found that using 85% Si<sub>0.66</sub>Sn<sub>0.34</sub> - 15 % graphite composites milled during 10 hours it was possible to obtain an initial capacity of ~1000 mAh g<sup>-1</sup>, which is retained up to ~80% after 50 cycles. Very recently, Hao et al.<sup>[36]</sup> prepared hierarchical macroporous Si/Sn composites, finding that a Si<sub>85</sub>Sn<sub>15</sub> sample delivers much higher specific capacity, superior cycling stability, and better rate capability as compared with Si<sub>80</sub>Sn<sub>20</sub> and pure Si anodes. From all the above it can be seen that the combination of Si, Sn and graphite is advantageous for the enhancement of the electrochemical performance of LIBs. However, and to the best of our knowledge, there is no systematic study aiming to find the best proportion of each material in the final composite, minimizing the drawbacks that present the alloy materials and buffering them with the inclusion of graphite thus allowing the highest specific capacity and cyclability of Sn/Si/graphite composite based anodes.

In this work we report -for the first time- a systematic study of Sn/Si/graphite composite materials prepared with variable amounts of each component. The composites were prepared via a simple high energy ball milling methodology using inexpensive Sn, Si and graphite micro-particulate powders. The obtained materials were characterized through X-ray powder diffraction and SEM microscopy and evaluated as anodes for LIBs. The electrochemical performance of the composites showed a strong dependence on the initial composition. The analysis of the charge/discharge curves and electrochemical impedance spectroscopy taken at different cycling stages revealed that the solid electrolyte interphase (SEI) formation is one of the key parameters that impact the performance of the anodes. The best results were obtained with Sn/Si/graphite composites containing

the same percentage (in weight) of each material, which exhibited specific capacities of 906.9 mAh g<sup>-1</sup> after 50 cycles at 1.5 A g<sup>-1</sup>.

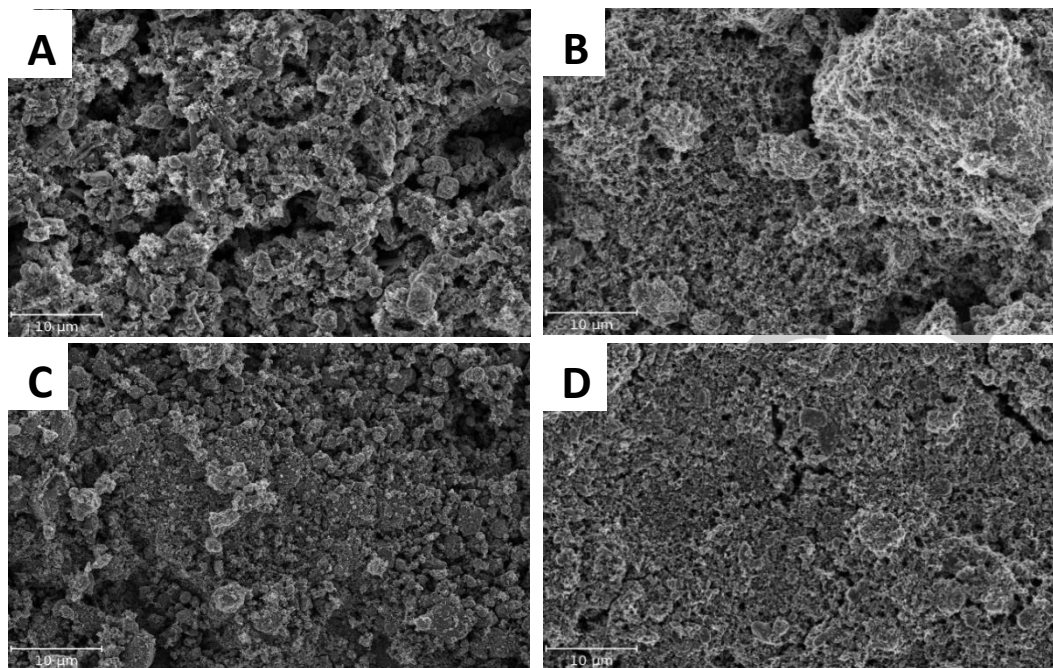
## Results and Discussion

Figure 1 shows the diffractograms of all the composites containing Sn, Si and graphite in their different compositions. For a better comparison, the XRD corresponding to the Si, Sn and graphite pure samples were added and their reference peaks were marked on the figure. All the signals were normalized by the highest signal. The diffractograms corresponding to mixtures containing only two components are shown in Figure S1.



**Figure 1.** X-Ray diffractograms for Si, graphite, Sn, Sn<sub>25</sub>Si<sub>25</sub>C<sub>25</sub>, Sn<sub>25</sub>Si<sub>50</sub>C<sub>25</sub>, Sn<sub>50</sub>Si<sub>25</sub>C<sub>25</sub> and Sn<sub>33</sub>Si<sub>33</sub>C<sub>33</sub>. For better interpretation of the peaks, the 2θ values of each pure component were marked with lines of different colors.

Si presents three main peaks at 28°, 47° and 56° corresponding to the (111), (220) and (311) planes, respectively.<sup>[37]</sup> In the case of graphite, the main peak is located at 26° and it is assigned to the (002) planes<sup>[38]</sup>. Other signals are also present but the previous one is the most intense. Lastly, Sn XRD shows signals at 30°, 32°, 44°, 45°, 55°, 62°, 64°, 72° and 73° due to (200), (101), (220), (211), (301), (112), (400), (321) and (420) planes, respectively.<sup>[30]</sup> All the milled mixtures containing Sn/Si/C reveal a peak at 26° – with different intensities – indicating partial amorphization of graphite in each sample. The lowest the peak intensity, the highest the amorphization suffered by graphite. It is also evident that the ternary mixtures show no shifts in the peak positions for Sn and Si relative to the corresponding pure reference patterns, indicating that the initial structure of the pristine materials is conserved. This observation is also supported by the absence of new signals revealing that there is no formation of new crystalline phases -chemical bonding- during the milling process.



**Figure 2.** SEM images of powder samples (A)  $\text{Sn}_{50}\text{Si}_{25}\text{C}_{25}$ , (B)  $\text{Sn}_{25}\text{Si}_{50}\text{C}_{25}$ , (C)  $\text{Sn}_{25}\text{Si}_{25}\text{C}_{50}$ , and (D)  $\text{Sn}_{33}\text{Si}_{33}\text{C}_{33}$ .

**Table 1.** Specific capacities at different number of cycles ( $Q_n$ ), capacity retention and faradaic efficiency (CE) for the studied anodes.

Anode	$Q_T^{(a)}$	$Q_1^{(a)}$	$Q_3^{(a)}$	$Q_{120}^{(a)}$	Capacity retention <sup>(b)</sup>	CE <sup>(c)</sup>
C	372	239.6	244.4	234.2	95.8	$99.9 \pm 0.5$
Si	3579	2825.1	2484.9	623.4	25.1	$98.7 \pm 0.3$
Sn	998	666.9	524.5	37.2	7.1	$94.8 \pm 0.3$
$\text{Sn}_{25}\text{Si}_{25}\text{C}_{50}$	1330	1861.2	950.8	651.4	68.5	$100.0 \pm 0.5$
$\text{Sn}_{25}\text{Si}_{50}\text{C}_{25}$	2132	2082.2	1457.8	929.1	63.7	$99.2 \pm 0.1$
$\text{Sn}_{50}\text{Si}_{25}\text{C}_{25}$	1486	1358.3	624.9	460.6	73.7	$99.8 \pm 0.2$
$\text{Sn}_{33}\text{Si}_{33}\text{C}_{33}$	1633	1499.5	1211.2	906.9	74.9	$99.8 \pm 0.1$

<sup>(a)</sup> $Q_T$ : theoretical capacity ( $\text{mAh g}^{-1}$ ) calculated according to Eq. 1,  $Q_n$ : specific discharge capacities determined at the  $n^{\text{th}}$  cycle, with  $n = 3, 50$  and  $120$  ( $\text{mAh g}^{-1}$ ). <sup>(b)</sup>Capacity retention: calculated as  $Q_{120}/Q_3$  – since 3 and 120 are measured at the same current (%). <sup>(c)</sup>CE: average coulombic efficiency calculated over 120 cycles (%). **Note:** data corresponding to the duets are summarized in Table S1.

SEM microscopy was used for the morphological characterization of the composites. Figure 2 shows the images of all the studied triads.  $\text{Sn}_{50}\text{Si}_{25}\text{C}_{25}$  (A) presents the most agglomerated morphology, followed by  $\text{Sn}_{25}\text{Si}_{50}\text{C}_{25}$  (B),  $\text{Sn}_{25}\text{Si}_{25}\text{C}_{50}$  (C) and  $\text{Sn}_{33}\text{Si}_{33}\text{C}_{33}$  (D). This indicates that as the amount of Sn increases, so does the agglomerations and size of

the composites, which may be related to its melting during the milling process. This observation is in good agreement with the morphology of pristine Sn powder (Figure S2 A), which shows a huge agglomeration by itself. Furthermore, the higher the concentration of graphite in the sample, the lower the agglomeration due to faster heat diffusion during milling.

All the materials were characterized by galvanostatic charge/discharge curves at three different specific currents during 120 cycles. The first three cycles were performed at 0.10 A g<sup>-1</sup> to ensure the formation of the SEI.<sup>[39]</sup> After that, the current was increased to 0.50 A g<sup>-1</sup> for 50 cycles and then to 1.50 A g<sup>-1</sup> for other 50 cycles, to analyze the electrochemical behavior under more demanding conditions, and finally restored to 0.5 A g<sup>-1</sup> to evaluate memory effects of the materials. Figure 3 compares the cycling data for all the tested triads (the comparison with the duets can be seen in Figure S3). Table 1 summarizes the electrochemical performances of all triads, including the theoretical capacity calculated as:

$$Q_T = X_{Sn}Q_{T,Sn} + X_{Si}Q_{T,Si} + X_CQ_{T,C} \quad (\text{Eq. 1})$$

where  $X_i$  represent the mass fraction of each material in the mixture and  $Q_{T,i}$ , the theoretical capacity of the corresponding pure element. The data of the blank Si, Sn and graphite are included for a better comparison and the data corresponding to the duets are summarized in Table S1. As it can be concluded from the values of Table 1, both Si and Sn precursors exhibited poor electrochemical performance, with a fast capacity decay, due to the large volume changes during the cycling process.

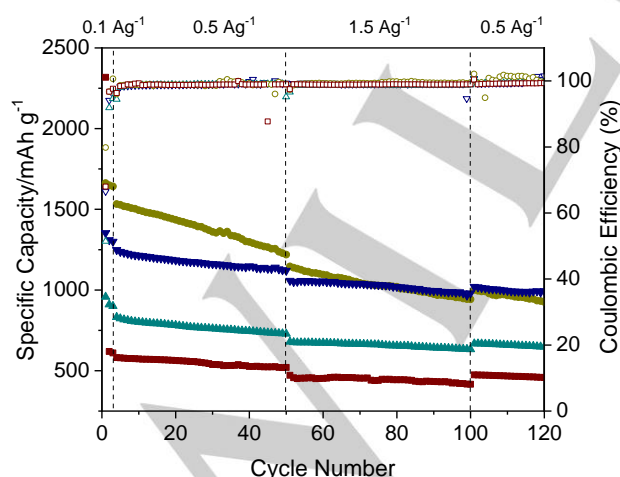


**Figure 3.** Discharge specific capacity of the cell using the different tested triads: Sn<sub>25</sub>Si<sub>25</sub>C<sub>50</sub> (▲), Sn<sub>25</sub>Si<sub>50</sub>C<sub>25</sub> (●), Sn<sub>50</sub>Si<sub>25</sub>C<sub>25</sub> (■) and Sn<sub>33</sub>Si<sub>33</sub>C<sub>33</sub> (▼).

The hollow symbols represent the coulombic efficiency of the respective samples.

As expected, the highest theoretical capacities correspond to the composites with the largest amount of Si: Sn<sub>33</sub>Si<sub>66</sub> and Si<sub>66</sub>C<sub>33</sub> (see Table S1). However, the high capacity obtained in the first cycle considerably diminishes in the following ones due to large volume changes leading to low capacity retention. This last value increases when graphite is present in the composite. Similar trends are observed for samples containing the same amount of Si and variable weight proportions of graphite and Sn (Sn<sub>66</sub>Si<sub>33</sub> vs. Si<sub>33</sub>C<sub>66</sub>; Sn<sub>25</sub>Si<sub>25</sub>C<sub>50</sub> vs. Sn<sub>50</sub>Si<sub>25</sub>C<sub>25</sub>). The capacity retention of the composites improved up to about 75% at cycle 120, when an equal mass ratio of each component (Sn<sub>33</sub>Si<sub>33</sub>C<sub>33</sub>) was used. However, not only the capacity retention improves. The initial coulombic efficiency (ICE) for all the analyzed triads were 74.1 %, 80.9 %, 68.6 % to 86.7 % for Sn<sub>25</sub>Si<sub>25</sub>C<sub>50</sub>, Sn<sub>25</sub>Si<sub>50</sub>C<sub>25</sub>, Sn<sub>50</sub>Si<sub>25</sub>C<sub>25</sub> and Sn<sub>33</sub>Si<sub>33</sub>C<sub>33</sub>, respectively. The highest ICE value for the Sn<sub>33</sub>Si<sub>33</sub>C<sub>33</sub> composite highlights one again an optimum mass ratio for attaining the best performance.

Figure 4 A and B show the differential capacity (dQ/dV) plots for Sn<sub>33</sub>Si<sub>33</sub>C<sub>33</sub> and Sn<sub>25</sub>Si<sub>50</sub>C<sub>25</sub> anodes, respectively, for the 3<sup>rd</sup>, 5<sup>th</sup> and 50<sup>th</sup> cycle. As a reference, the dQ/dV profiles of the pure components Sn, Si and graphite are included in Figure 4 C-E, ball-milled in the same conditions as the composites.

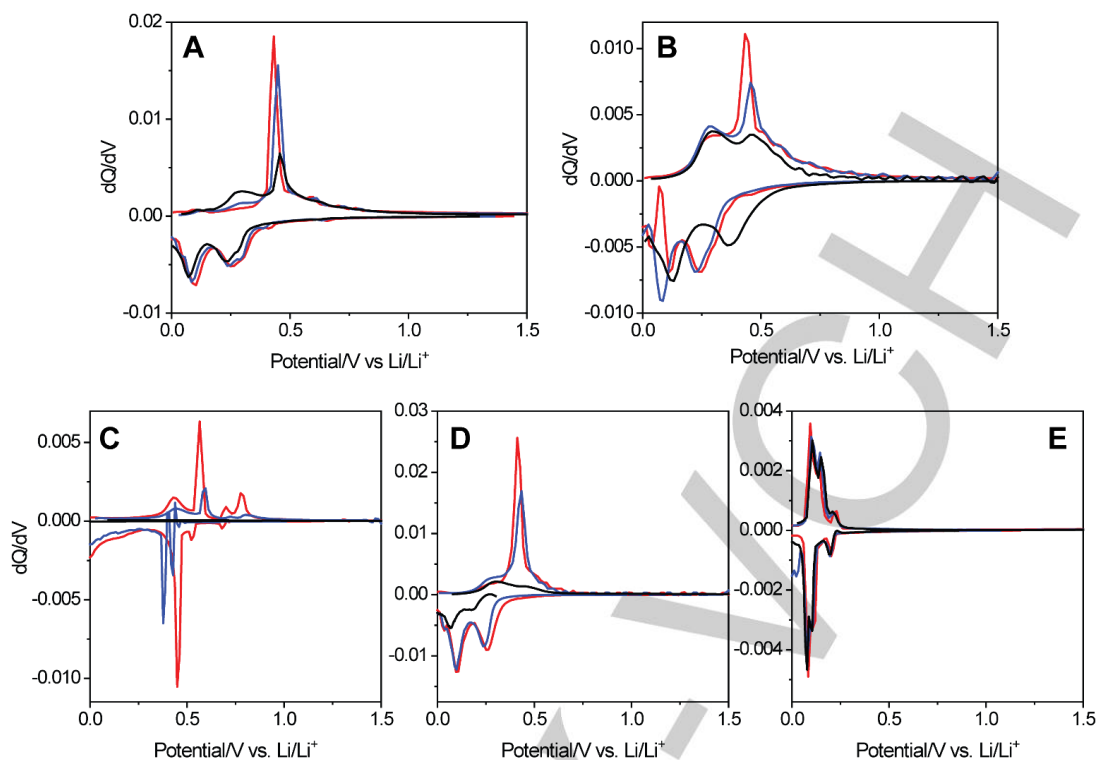


**Figure 4.** Differential charge plots for the 3<sup>rd</sup> (red), 5<sup>th</sup> (blue) and 50<sup>th</sup> (black) cycles measured using Sn<sub>33</sub>Si<sub>33</sub>C<sub>33</sub> (A), Sn<sub>25</sub>Si<sub>50</sub>C<sub>25</sub> (B), Sn (C), Si (D) and graphite (E) as anode electrodes.

The cathodic part of the third cycle of Sn<sub>33</sub>Si<sub>33</sub>C<sub>33</sub> (A) and Sn<sub>25</sub>Si<sub>50</sub>C<sub>25</sub> (B) presents several peaks at 0.660, 0.411, 0.304, 0.248 V and 0.097 V. The peaks at 0.660 V and 0.411 V are due to the formation of Li-Sn alloys<sup>[40]</sup>, while the reduction peaks at 0.304 and 0.248 V can be related with Si lithiation.<sup>[41]</sup> The last signal at 0.097 V can be assigned to the transformation of Li<sub>x</sub>Si to Li<sub>15</sub>Si<sub>4</sub> and also to graphite lithiation, which occurs at similar potentials. On the other hand, during the anodic process, the peaks around 0.100 V correspond to graphite delithiation. The oxidation peak at 0.431 V and its corresponding shoulder at higher potentials can be attributed to both Si and Sn delithiation.<sup>[40,41]</sup> The three subsequent peaks observed at 0.600 V, 0.704 V and 0.773 V may be assigned to Sn delithiation.<sup>[40]</sup> The appearance of the peaks is consistent with the profiles of the pure components shown in Figure 4 C-E and is an indication

that Si, Sn and graphite are fully participating in the whole electrochemical lithiation and delithiation processes. The evolution of the dQ/dV profiles in A and B reveals significant changes in the peaks corresponding to Si from the third to the 50<sup>th</sup> cycle. During the anodic segment (Figure 4 A), there is a remarkable decrease of the peak centered at ~-0.43 V and an increase of a broad signal at ~-0.26 V. This peak is associated to the delithiation of the crystalline phase Li<sub>15</sub>Si<sub>4</sub> and its reduction upon cycling shows that there is less formation of this phase during the cathodic cycle as a consequence of Si amorphization. The formation of Li<sub>15</sub>Si<sub>4</sub> at very low potentials during the lithiation accounts for the biggest volume changes in the alloying mechanism of Si. The changes in the volume are the ones that explain the loss of active material as a consequence of particle cracking and continuous formation of SEI upon anode cycling.

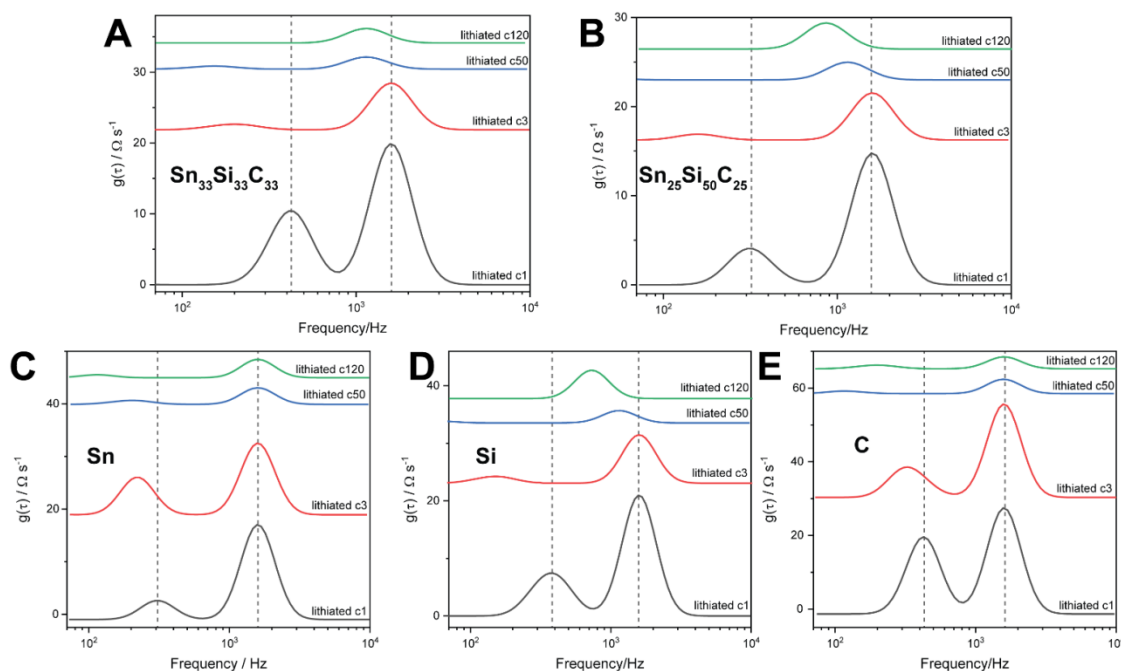


**Figure 5.** DRT plots of the EIS of  $\text{Sn}_{33}\text{Si}_{33}\text{C}_{33}$  (A),  $\text{Sn}_{25}\text{Si}_{50}\text{C}_{25}$  (B), Sn (C), Si (D) and graphite (E) anode electrodes. The plots correspond to the EI spectra taken at the 100% lithiated state ( $E = 0.010$  V) at the first (black line), third (red line), 50<sup>th</sup> (blue line) and 120<sup>th</sup> cycle (green line). A zoom of the 50<sup>th</sup> and 120<sup>th</sup> cycles for each electrode can be found in the Supporting Information, Figure S4.

A hint of this electrochemical behavior can be found in the electrochemical impedance spectra (EIS) for the different samples. As there are many electrochemical processes that contribute to the total anodes impedance (*i.e.* 2 alloying reactions + 1 intercalation material + surface phenomena), for better visualization, the EIS were resolved through the method of the distribution of relaxation times (DRT). The latter is a helpful approach for the derivation of distinguishable time constants in EIS as it significantly increases its resolution.<sup>[42,43]</sup> The DRT plots of the EIS measured at the lithiated state of the first, third, 50<sup>th</sup> and 120<sup>th</sup> cycle are shown in Figure 5.

All the DRT plots for the first lithiated cycle of Figure 5 display two peaks, in the range between  $10^2$  and  $10^4$  Hz, representing two different time constants. The high frequency process is associated to the surface resistance at the electrolyte-electrode interface (SEI formation and Li-ion solid diffusion) while the low frequency one, corresponds to the charge transfer of Li-ions with the active material.<sup>[44]</sup> For each

electrode, the area of the high frequency surface process is bigger than the lower frequency charge transfer-related one. As the area under the peaks is directly proportional to the resistance of the process<sup>[45]</sup>, the former is the one that dominates the kinetics for all the electrodes. For Sn and graphite anodes (panels C and E) the frequency of the SEI-related process remains constant throughout cycling and the charge transfer one downshifts. For the Si anode (panel D) both of the processes decrease in frequency, while the charge transfer process almost disappear after 120 cycles. In the case of the composite anodes,  $\text{Sn}_{25}\text{Si}_{50}\text{C}_{50}$  exhibits a marked drop in the frequency of the SEI process (as in the case of the Si anode). Although  $\text{Sn}_{33}\text{Si}_{33}\text{C}_{33}$  also displays a downshift, it is less marked than in the case of the previous. The decrease in the characteristic frequency is related to a sluggishness in the electrochemical process. The volume changes occurring during cycling are known to generate a continuous cracking and reformation of the SEI continuously growing throughout cycling

<sup>[46]</sup>, which could explain the fact that the SEI surface related process lags. Furthermore, and as in the case of the Si anode, after the 50<sup>th</sup> cycle this process dominates the global kinetics of the electrode reaction for the composites, implying that this is a characteristic feature of Si-based anodes. Nonetheless, the less marked decrease in the frequency for the Sn<sub>33</sub>Si<sub>33</sub>C<sub>33</sub> shows a slower degradation of the SEI which explains why this composite

anode presents a better capacity retention as opposed to Sn<sub>25</sub>Si<sub>50</sub>C<sub>25</sub> (Figure 3). In this sense, although the increase in the amount of graphite and tin in the composite yields a lower specific capacity, it produces a positive buffering effect, which can be related to better particle connectivity, better electronic conductivity and/or smaller volumetric change of the material.

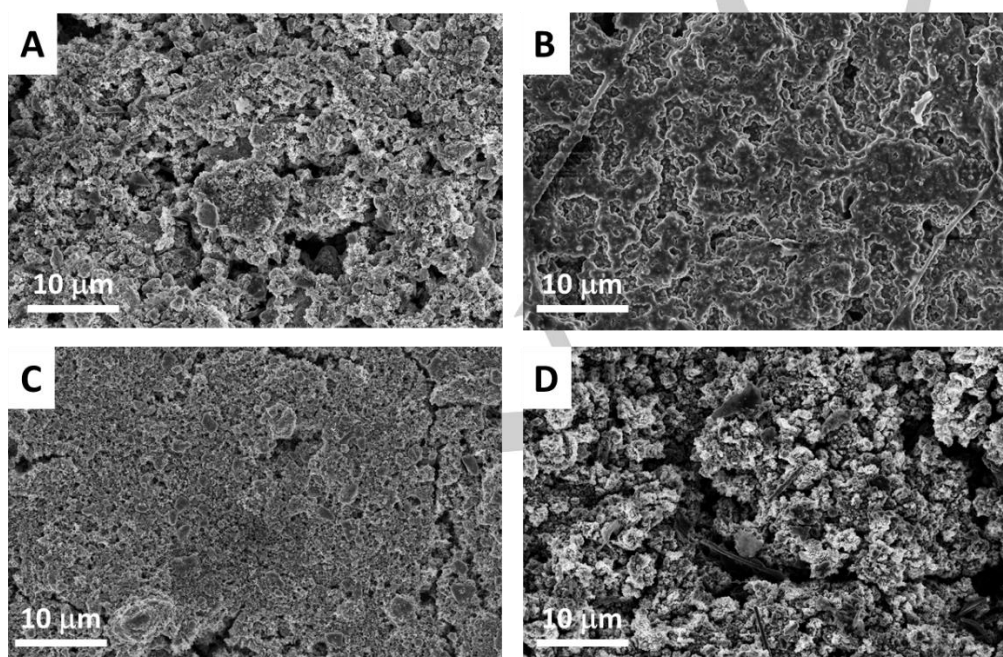


**Figure 6.** SEM images for the Sn<sub>25</sub>Si<sub>50</sub>C<sub>25</sub> (A, B) and Sn<sub>33</sub>Si<sub>33</sub>C<sub>33</sub> (C, D) composites anodes, before (A, C) and after (B, D) cycling.

SEM images support the evidence found by EIS. Figure 6 presents the representative SEM images of the electrodes surface for the pristine and cycled (after 120 discharge/charge cycles) composite anodes Sn<sub>25</sub>Si<sub>50</sub>C<sub>25</sub> and Sn<sub>33</sub>Si<sub>33</sub>C<sub>33</sub> (A, B and C, D respectively). As can be seen, electrodes prepared with Sn<sub>25</sub>Si<sub>50</sub>C<sub>25</sub> present a more inhomogeneous distribution than Sn<sub>33</sub>Si<sub>33</sub>C<sub>33</sub>, in good agreement with the major granulates observed for the pristine powders of Figure 2 B and D. After 120 cycles (Figure 6 B and D), the electrodes are covered by the SEI, evidenced by the smoother edges. A thin and homogeneous SEI layer can be seen at the Sn<sub>33</sub>Si<sub>33</sub>C<sub>33</sub> anode while the cycled

Sn<sub>25</sub>Si<sub>50</sub>C<sub>25</sub> shows a thicker and non-uniform organic coating. In this way, SEM images confirm that the SEI becomes thicker for increasing Si content in the composites, and therefore the surface resistance becomes the phenomenon controlling the overall electrochemical process as observed in EIS measurements<sup>[47]</sup>.

To graphically summarize the obtained results, we present ternary graphs of specific capacity at the 120<sup>th</sup> cycle and capacity retention as function of the percentage composition of each material (Figure 7 A and B, respectively). The ternary

graphs were constructed including all the measured data for each composition and filling the gaps with cubic splines.

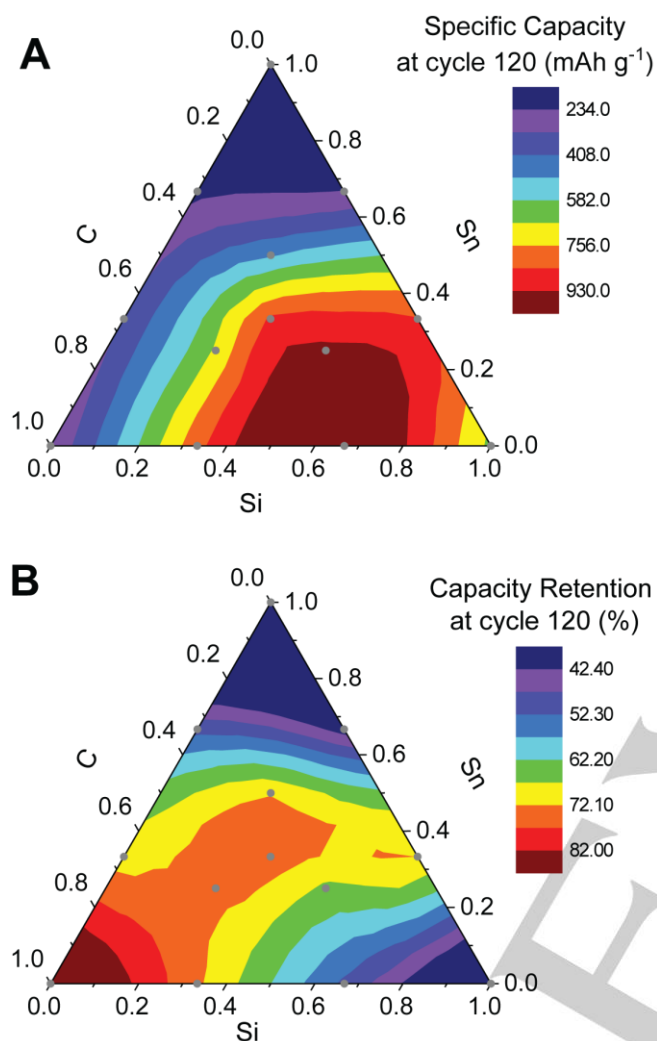


**Figure 7.** Specific capacity at the 120<sup>th</sup> cycle in terms of the composition of Si, Sn and graphite (A). Capacity retention at cycle 120<sup>th</sup> relative to the 3<sup>rd</sup> cycle (B). Points indicate the studied compositions.

As seen in Figure 7, the samples with the highest capacity are found in the middle-bottom of the diagram, while capacity retention is better towards the bottom-left part of the diagram. Therefore, as expected, graphite-rich electrodes yield the best capacity retention while Si-rich ones deliver the greatest capacities. The capacity drop when the current density is changed from 0.5 A g<sup>-1</sup> to 1.5 A g<sup>-1</sup>,  $C_{drop}$ , was calculated and plotted as function of the Sn/Si/C composition (Figure 8).

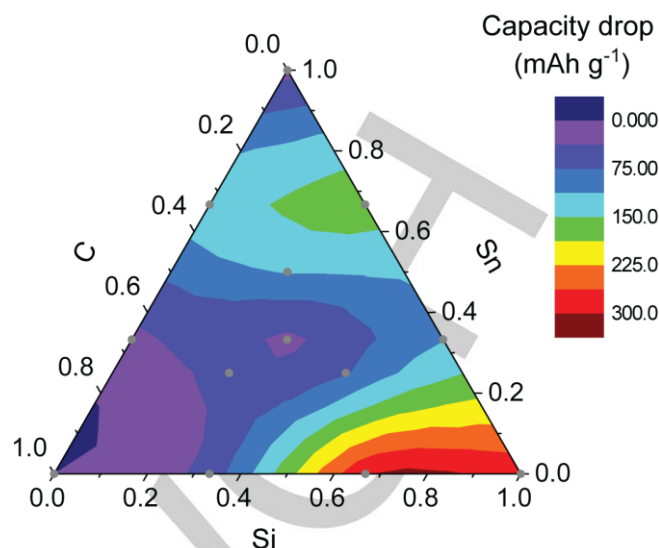


**Figure 8.** Capacity drop (mAh g<sup>-1</sup>), registered when current is increased from 0.50 A g<sup>-1</sup> to 1.50 A g<sup>-1</sup>.

Although in Figure 6 and 7 the best performances are rather located at the center or left-bottom region of the ternary composition graph (low Sn content), the lowest capacity drops at 1.50 A g<sup>-1</sup> are obtained for graphite-rich samples, approaching the 100% in the graphite vertex and the center of the graph. On the other hand, the highest capacity drop at 1.50 A g<sup>-1</sup> is obtained for samples containing higher amounts of Si - at the bottom-right corner - in good agreement with the high volume changes suffered by this material. In order to put together into an equation the three criteria chosen here to define the efficiency  $E$  of a material taking in consideration the specific capacity at 120<sup>th</sup> cycle, the capacity retention and the capacity drop when increasing the current density, we propose the following equation (Eq. 2):

$$E = w_1 \left( \frac{Q_{120} - Q_{120}^{\min}}{Q_{120}^{\max} - Q_{120}^{\min}} \right) + w_2 \left( \frac{C_{ret,120} - C_{ret,120}^{\min}}{C_{ret,120}^{\max} - C_{ret,120}^{\min}} \right) + w_3 \left( \frac{C_{drop} - C_{drop}^{\max}}{-C_{drop}^{\min} - C_{drop}^{\max}} \right) \quad (\text{Eq. 2})$$

where  $Q_{120}$  is the specific discharge capacity after 120 cycles,  $C_{ret,120}$  is the capacity retention after 120 cycles and  $C_{drop}$  is the capacity drop when the current density is changed from 0.50 A

$\text{g}^{-1}$  to  $1.50 \text{ A g}^{-1}$ . The upper indices in this equation indicate maximum (max) and minimum (min) values respectively among the samples considered and  $w_1$ ,  $w_2$  and  $w_3$  are weight factors that fulfill the condition:  $w_1 + w_2 + w_3 = 1$ . The meaning of Eq. 2 is straightforward: each term in parenthesis may range between 0 and 1, indicating the corresponding value the suitability of the material according to the property measured. The weight factors may be chosen to emphasize the contribution of each property to the desired efficiency. For example, choosing the set  $w_1 = 1, w_2 = 0, w_3 = 0$  to focus on the material with the best  $Q_{120}$ , yields that the optimum material would be  $\text{Sn}_{25}\text{Si}_{50}\text{C}_{25}$ . On the other hand, choosing  $w_1 = 0, w_2 = 1, w_3 = 0$  or  $w_1 = 0, w_2 = 0, w_3 = 1$  would yield graphite as the best candidate. On the other hand, if we set an equivalent weight for all properties,  $w_1 = w_2 = w_3 = 1/3$ , we get the ranking for the materials given in Table 2.

**Table 2.** Efficiency, defined according to Eq. 2, of the different composite Sn – Si – graphite anodes essayed.

Sample	E
$\text{Sn}_{33}\text{Si}_{33}\text{C}_{33}$	0.871
$\text{Si}_{33}\text{C}_{66}$	0.794
$\text{Sn}_{25}\text{Si}_{50}\text{C}_{25}$	0.768
$\text{Sn}_{33}\text{Si}_{66}$	0.744
C	0.731
$\text{Sn}_{25}\text{Si}_{25}\text{C}_{50}$	0.727
$\text{Sn}_{33}\text{C}_{66}$	0.636
$\text{Sn}_{50}\text{Si}_{25}\text{C}_{25}$	0.591
$\text{Si}_{66}\text{C}_{33}$	0.508
$\text{Sn}_{66}\text{C}_{33}$	0.408
$\text{Sn}_{66}\text{Si}_{33}$	0.325
Sn	0.301
Si	0.268

Thus, from Table 2, we find that combining with equivalent weights the criteria of high specific capacity ( $w_1$ ), good capacity retention after 120 cycles ( $w_2$ ) and low capacity drop when increasing loading current ( $w_3$ ), the best condition is found at the center of the ternary plots, coinciding with the tested sample  $\text{Sn}_{33}\text{Si}_{33}\text{C}_{33}$ . These results show that the amounts of Si, Sn and graphite in the samples play a crucial role. While Si provides a good capacity, Sn is in charge of the electrical connection and microcrystalline graphite buffers volume changes during lithiation, producing a synergic effect that results in a very promising material for application in LIBs.

In addition, the electrochemical performance of the ball-milled prepared  $\text{Sn}_{33}\text{Si}_{33}\text{C}_{33}$  anode was compared to a homologous one prepared by simple physical mixture in an agate mortar (Figure S5). Sn, Si and graphite were used maintaining the same weight proportion and electrode's preparation methodology as the ball milled sample. The anode based on the ball-milled high energy preparation method presents a better performance, less capacity fade and greater capacities than the anode prepared by simple physical mixture, indicating that the close contact and interaction between the three components is highly beneficial and necessary for attaining a good cyclability.

## Conclusions

In the present work we have implemented a straightforward ball-milling procedure to prepare Sn/Si/graphite composites to be used as anode in lithium-ion batteries. A systematic study of lithium-ion storage was undertaken using different compositions. The figures of merit analyzed were the capacity after 120 cycles, capacity retention after this number of cycles and capacity drop upon a 3-fold charging current increase. From all the compositions analyzed and giving equal weight to the previous figures of merit, the most promising appears to be  $\text{Sn}_{33}\text{Si}_{33}\text{C}_{33}$  as mixture for anodes of LIBs, showing the

importance of considering the percentage of the different materials in the final electrode composite.

## Experimental Section

### Materials and chemicals

Sn powder (100 mesh) was from Alfa Aesar. Si powder (325 mesh) and polyacrylic acid (PAA) were purchased from Sigma-Aldrich. Graphite Micrograf was from Nacional de Grafito (mean particle size ~2  $\mu\text{m}$ ). TIMCAL carbon superP was from MTI Technologies. Other reagents were battery grade and were used without further purification.

### Synthesis and characterization of materials

All powders were handled inside an argon filled glove box ( $\text{H}_2\text{O}$  and  $\text{O}_2$  content < 1ppm). The composites were prepared by one-step mechanical ball milling. For that, commercial Sn, Si and graphite powders were mixed in a variable proportion and ball-milled for 6 hours in a Fritsch Pulverisette 7 (Hard stainless steel balls, 7 mm diameter). The ball-milling treatment was carried out at room temperature and the weight ratio of milling balls to mixture was kept at 35:1 with a milling rate of 400 rpm. To reduce temperature rises during the milling, the process was done at intervals of 30 min with a 30 min rest between each cycle and the vials were never opened during the whole treatment. Once the milling process was completed, the samples were collected and stored in the glove box. Each sample was labeled according to its initial composition as  $\text{Sn}_x\text{Si}_y\text{C}_z$ , where x, y and z represent weight composition of each material, respectively. Table 3 summarizes the tested active materials compositions.

**Table 3.** Anodes notation and active materials mass fractions.

Nomenclature	Sn content (wt. %)	Si content (wt. %)	Graphite content (wt. %)
Sn	100	0	0
Si	0	100	0
C	0	0	100
$\text{Sn}_{33}\text{Si}_{66}$	33	66	0
$\text{Sn}_{66}\text{Si}_{33}$	66	33	0
$\text{Sn}_{33}\text{C}_{66}$	33	0	66

$\text{Sn}_{66}\text{C}_{33}$	66	0	33
$\text{Si}_{33}\text{C}_{66}$	0	33	66
$\text{Si}_{66}\text{C}_{33}$	0	66	33
$\text{Sn}_{25}\text{Si}_{25}\text{C}_{50}$	25	25	50
$\text{Sn}_{50}\text{Si}_{25}\text{C}_{25}$	50	25	25
$\text{Sn}_{33}\text{Si}_{33}\text{C}_{33}$	33	33	33

The structural characterization of the composites was done by X-ray diffraction (XRD) using a Philips PW1800/10 diffractometer operated at 40 kV and 30 mA with a Cu-K $\alpha$  radiation source and complemented with scanning electron microscopy (SEM) images obtained with a field emission scanning electron microscope FE-SEM, Sigma Zeiss (LAMARX facilities) working at 5 kV.

### Electrochemical testing

In order to evaluate the electrochemical properties, electrodes were prepared by milling process mixing 80 wt.% of the active material with 10 wt.% TIMCAL carbon superP and 10 wt.% polyacrylic acid (PAA) as binder. 0.1 M citric acid buffer solution pH 3.00 served as dispersing medium. All the components were mixed by using 5 min of ball milling at 600 rpm. The well-mixed slurry was cast onto a copper foil using a doctor blade. The electrodes were dried in an oven at 80  $^{\circ}\text{C}$  for 2 hours and then punched into a 1.13  $\text{cm}^2$  disk and stored into the glove box. The areal mass loading of active material was ~1.2  $\text{mg cm}^{-2}$  for every tested material.

A Swagelok T type cell was used for the electrochemical characterization of the anodes. Lithium foils were used as both, counter and reference electrodes and glass fiber as separator. A liquid electrolyte consisting in 1.00 M  $\text{LiPF}_6$  and 10 wt.% fluoroethylene carbonate (FEC) in ethylene carbonate/ethylmethyl carbonate (EC/EMC) 1:1 v/v was used. All Swagelok cells were cycled under constant current charge/discharge conditions using a galvanostat (Arbin instruments, USA). Tests were conducted employing three different constant current densities: 0.10  $\text{A g}^{-1}$ , 0.50  $\text{A g}^{-1}$  and 1.50  $\text{A g}^{-1}$ . All cells were cycled in the voltage range 0.01 - 3.00 V. Specific capacities (expressed in  $\text{mAh g}^{-1}$ ) and current densities were calculated in terms of the total mass of active material ( $\text{Sn}_x\text{Si}_y\text{C}_z$ ).

Electrochemical Impedance Spectroscopy (EIS) was carried out at selected cycles at the full lithiated state. The perturbation potential was 10 mV while the frequency range was between  $10^4 - 1$  Hz. For the

analysis of distribution of relaxation times (DRT) the *DRTtools* toolbox for MATLAB<sup>®</sup> was used. [48]

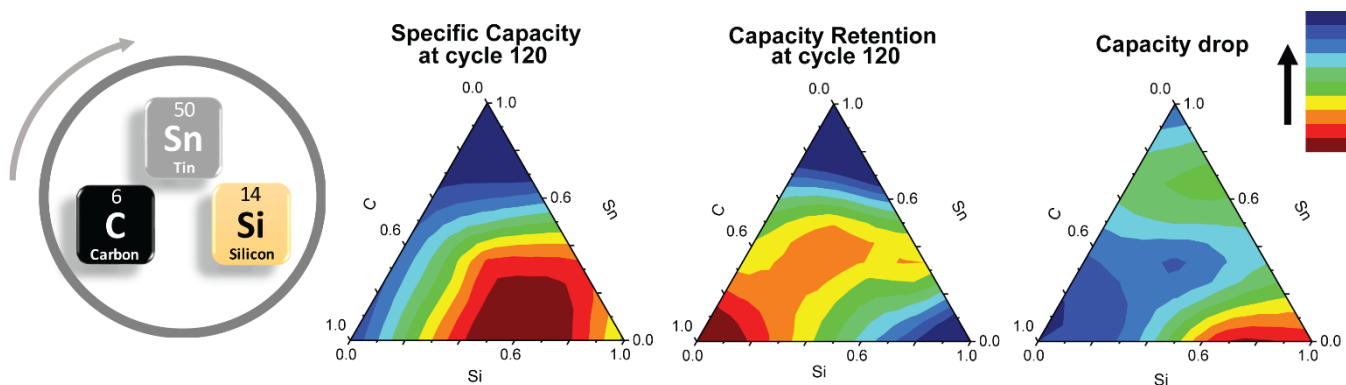
## Acknowledgements

The authors acknowledge partial financial support for this research from grants PIO Conicet-YPF 3855/15, PID Conicet-11220150100624, Program BID-Foncyt (PICT-2015-1605), Program BID-Foncyt (PICT-2016-0718) and SeCyT of the Universidad Nacional de Córdoba and YPF-Tecnología (Y-TEC), Argentina.

**Keywords:** tin • silicon • graphite • composite anodes • lithium-ion batteries

- [1] Z. Yang, J. Zhang, M. C. W. Kintner-Meyer, X. Lu, D. Choi, J. P. Lemmon, J. Liu, *Chem. Rev.* **2011**, *111*, 3577.
- [2] Y. Ashraf Gandomi, D. S. Aaron, J. R. Houser, M. C. Daugherty, J. T. Clement, A. M. Pezeshki, T. Y. Ertugrul, D. P. Moseley, M. M. Mench, *J. Electrochem. Soc.* **2018**, *165*, A970.
- [3] J. Leadbetter, L. G. Swan, *J. Power Sources* **2012**, *216*, 376.
- [4] B. Scrosati, J. Garche, *J. Power Sources* **2010**, *195*, 2419.
- [5] D. Lin, Y. Liu, Y. Cui, Reviving the lithium metal anode for high-energy batteries. *Nat. Nanotechnol.* **2017**, *12*, 194–206.
- [6] B. Li, Y. Wang, S. Yang, *Adv. Energy Mater.* **2018**, *8*, 1702296.
- [7] T. Jiang, F. Bu, X. Feng, I. Shakir, G. Hao, Y. Xu, *ACS Nano* **2017**, *11*, 5140.
- [8] M. V. Bracamonte, E. N. Primo, G. L. Luque, L. Venosta, P. G. Bercoff, D. E. Barraco, *Electrochim. Acta* **2017**, *258*, 192.
- [9] Y. Zhao, X. Li, B. Yan, D. Xiong, D. Li, S. Lawes, X. Sun, *Adv. Energy Mater.* **2016**, *6*, 1502175.
- [10] J. Yan, Z. Bin, L. Zhenda, L. Nian, Z. Jia, *Adv. Energy Mater.* **2017**, *7*, 1700715.
- [11] H. Gao, L. Xiao, I. Plümel, G.-L. Xu, Y. Ren, X. Zuo, Y. Liu, C. Schulz, H. Wiggers, K. Amine, Z. Chen, *Nano Lett.* **2017**, *17*, 1512.
- [12] Q. Xu, J.-K. Sun, Y.-X. Yin, Y.-G. Guo, *Adv. Funct. Mater.* **2018**, *28*, 1705235.
- [13] J. Ryu, D. Hong, H.-W. Lee, S. Park, *Nano Res.* **2017**, *10*, 3970.
- [14] J. Beibei, H. Yanjie, L. Bo, Z. Shiqiang, W. Shun, H. Yan-Bing, L. Zhiqun, *Angew. Chemie Int. Ed.* **2017**, *56*, 1869.
- [15] Y. Li, A. M. Levine, J. Zhang, R. J. Lee, A. K. Naskar, S. Dai, M. P. Paranthaman, *J. Appl. Electrochem.* **2018**, *48*, 811.
- [16] S. Smrekar, M. E. Zoloff Michoff, J. E. Thomas, C. A. Calderón, L. M. Farigliano, A. Visintin, E. P. M. Leiva, D. E. Barraco, *J. Solid State Electrochem.* **2018**, *22*, 1721.
- [17] D. Liu, Z. jiao Liu, X. Li, W. Xie, Q. Wang, Q. Liu, Y. Fu, D. He, *Small* **2017**, *13*, 1702000.
- [18] D. Yang, J. Shi, J. Shi, H. Yang, *Electrochim. Acta* **2018**, *259*, 1081.
- [19] M. N. Obrovac, L. Christensen, *Electrochem. Solid-State Lett.* **2004**, *7*, A93.
- [20] L. Y. Yang, H. Z. Li, J. Liu, Z. Q. Sun, S. S. Tang, M. Lei, *Sci. Rep.* **2015**, *5*, 10908.
- [21] M. Ko, S. Chae, J. Ma, N. Kim, H. W. Lee, Y. Cui, J. Cho, *Nat. Energy* **2016**, *1*, 16113.
- [22] R. Dash, S. Pannala, *Sci. Rep.* **2016**, *6*, 27449.
- [23] R. Zhou, R. Fan, Z. Tian, Y. Zhou, H. Guo, L. Kou, D. Zhang, *J. Alloys Compd.* **2016**, *658*, 91.
- [24] S. Okashy, S. Luski, Y. Elias, D. Aurbach, *J. Solid State Electrochem.* **2018**, *22*, 3289.
- [25] J. Nzabahimana, P. Chang, X. Hu, *J. Mater. Sci.* **2019**, *54*, 4798.
- [26] J. Nzabahimana, Z. Liu, S. Guo, L. Wang, X. Hu, *ChemSusChem* **2020**, *13*, 1923.
- [27] S. Goriparti, E. Miele, F. De Angelis, E. Di, R. Proietti, C. Capiglia, *J. Power Sources* **2014**, *257*, 421.
- [28] H. Wu, Y. Cui, *Nano Today* **2012**, *7*, 414.
- [29] M. Gu, Y. He, J. Zheng, C. Wang, *Nano Energy* **2015**, *17*, 366.
- [30] I. S. Kim, G. E. Blomgren, P. N. Kumta, *Electrochem. Solid-State Lett.* **2004**, *7*, 1.
- [31] A. Kraysberg, N. Seizin, Y. Ein-Eli, *J. Solid State Electrochem.* **2018**, *22*, 3303.
- [32] W. J. Zhang, *J. Power Sources* **2011**, *196*, 13.
- [33] M. Kawasaki, V. Laokawee, T. Sarakonsri, T. Hashizume, M. Shiojiri, *J. Appl. Phys.* **2016**, *120*.
- [34] M. A. Al-Maghrabi, J. S. Thorne, R. J. Sanderson, J. N. Byers, J. R. Dahn, R. A. Dunlap, *J. Electrochem. Soc.* **2012**, *159*, A711.
- [35] N. L. Rock, P. N. Kumta, *J. Power Sources* **2007**, *164*, 829.
- [36] Q. Hao, J. Hou, J. Ye, H. Yang, J. Du, C. Xu, *Electrochim. Acta* **2019**, *306*, 427.
- [37] E. A. Odo, D. T. Britton, G. G. Gonfa, M. Harting, *African Rev. Phys.* **2012**, *7*, 45.
- [38] G. Sun, X. Li, Y. Qu, X. Wang, H. Yan, Y. Zhang, *Mater. Lett.* **2008**, *62*, 703.
- [39] U. S. Vogl, S. F. Lux, E. J. Crumlin, Z. Liu, L. Terborg, M. Winter, R. Kostecki, **2015**, *162*, 603.
- [40] J. L. Lorie Lopez, P. J. Grandinetti, A. C. Co, *J. Mater. Chem. A* **2019**, *7*, 10781.
- [41] K. Ogata, E. Salager, C. J. Kerr, A. E. Fraser, C. Ducati, A. J. Morris, S. Hofmann, C. P. Grey, *Nat. Commun.* **2014**, *5*, 3217.
- [42] T. H. Wan, M. Saccoccio, C. Chen, F. Ciucci, *Electrochim. Acta* **2015**, *184*, 483.
- [43] J. Illig, J. P. Schmidt, M. Weiss, A. Weber, E. Ivers-Tiffée, *J. Power Sources* **2013**, *239*, 670.
- [44] M. Steinhauer, T. Diemant, C. Heim, R. Jürgen Behm, N. Wagner, K. Andreas Friedrich, *J. Appl. Electrochem.* **2017**, *47*, 249.
- [45] T. P. Heins, N. Schlüter, S. T. Ernst, U. Schröder, *Energy Technol.* **2020**, *8*, 1900279.
- [46] J. Shin, T.-H. Kim, Y. Lee, E. Cho, *Energy Storage Mater.* **2020**, *25*, 764.
- [47] E. Radvanyi, K. Van Havenbergh, W. Porcher, S. Jouanneau, J.-S. Bridel, S. Put, S. Franger, *Electrochim. Acta* **2014**, *137*, 751.
- [48] DRTTOOLS.

## Entry for the Table of Contents



Composite electrodes were made from ball-milled **silicon**, **carbon** and **tin**. The mixture of these active materials aims to combine high capacity, good electrical conductivity and stability during the anode cycling. In this work we study systematically how the electrochemical behavior is affected by the weight proportion of each component in the mixture and we define a criterion to evaluate the performance of the composite anodes.